The International Journal of Advanced Manufacturing Technology
https://doi.org/10.1007/s00170-022-08988-6

ORIGINAL ARTICLE

Constrained abrasive jet polishing with a tangentially aligned nozzle shroud

Qiaoling Yuan[1,2] · **Xun Chen**[2] · **Donghui Wen**[1]

Received: 9 November 2021 / Accepted: 23 February 2022

Abstract

In order to improve surface polishing quality and efficiency for hard and brittle components, a novel nozzle with specifically designed shroud was proposed for an abrasive jet polishing process. The removal mechanism of the abrasive jet under such a nozzle was investigated by simulating the jet flow in the interaction area of the nozzle shroud and workpiece. The simulation results show that the speed of the abrasive jet increases greatly by the shroud and the direction of the jet is aligned near parallel to the workpiece surface to minimize impact damage to workpiece surface. The constrained abrasive jet polishing (CAJP) experiments were conducted on the quartz glass component, a typical hard and brittle material, showing that the material removal mainly relied on the shearing and scratching of the workpiece surface rather than the mechanical shock impacts, which is consistent with the simulation findings.

Keywords Abrasive jet machining · Nozzle · K9 optic glass · Removal mechanism

Abbreviations

A_M	Total flow cross section area
A_{Out}	Area of the annular section
c	Perimeter of the cross-section of the fluid contact to solid region
C	Variant of the blending function defined in Eq. (18)
d	Diameter of the channel hole
d_H	Hydraulic diameter
D_2	Inner diameter of the annular outlet
D_3	Outer diameter of the annular outlet
D^+	Positive portion of the orthogonal divergence term of Eq. (7)
$f_{friction}$	Friction force
F_1	Switching function in the near wall region
F_2	Blending function for boundary-layer flows and zero for free shear layers.
F_{motor}	Push force of the motor
G	Gravity of the polish tool
H_f	Hardness of the workpiece
H_p	Hardness of the abrasive
k	Turbulence kinetic energy
k_1, k_2, k_3, k_p	Coefficients of the Preston formula
P_{fluid}	Inlet fluid pressure
Re_0	Reynolds number
S_{ij}	Components of the mean strain tensor
t	Time
T	Abrasion process time
u_i,u_j,u_k	Mean velocity components in the x-, y- and z-directions
ν	Kinematic viscosity of the abrasive flow
v_0	Average speed of the jet at the exit slit
ν_t	Vortex coefficient
x	Orifice gap
x_i,x_j,	x_k Local Cartesian coordinates
y	Shortest distance from the current point to the physical plane
α	Inject angle
α_1	Constant in the transport equation for the turbulent shear stress
β^*, β	Empirical constants of the SST model [28]
$\beta_{i,1}$	Constants in the original k – ω model
$\beta_{i,2}$	Constants in the transformed k – ε model
γ	Intermittent factor

✉ Xun Chen
X.Chen@ljmu.ac.uk

[1] Key Laboratory of Special Purpose Equipment and Advanced Manufacturing Technology (Ministry of Education), ZheJiang University of Technology, Hang-Zhou 310014, China

[2] General Engineering Research Institute, Faculty of Engineering and Technology, Liverpool John Moores University, Liverpool L3 3AF, UK

Published online: 14 March 2022

γ_1	Constants in the original k − ω model
γ_2	Constants in the transformed k − ε model
Γ_k	Effective diffusion term of the k
Γ_ω	Effective diffusion term of the ω
ε	Dissipation rate of turbulent kinetic energy
θ_1,θ_2	Turn angle
μ	Dynamic viscosity of the abrasive flow
μ_t	Turbulent viscosity
ρ	Density
σ_k	Turbulent Prandtl numbers for k
σ_ω	Turbulent Prandtl numbers for ω
τ_{ij}	Shear stress
ϕ	Corresponding constant in the SST model
ϕ_1	Constants in the original k − ω model
ϕ_2	Constants in transformed k − ε model
ω	Specific dissipation rate
Ω	Absolute value of the vorticity

1 Introduction

Ever increased challenges in the fields of energy, optics and medicine increased the use of hard and brittle materials, such as optical glass, optical crystals, and engineering ceramics, etc. to meet the requirement for the exaltation of optical resolution, the reduction of scattering loss, the enhancement of damage-resistance threshold, and the guarantee of a reliable performance in a critical precision application with higher quality demands in both geometrical accuracy and surface integrity [1]. Considering complex geometry surface, it is highly desirable to apply a super-precision machining technique to secure higher accuracy, better integrity quality and higher productivity. The employed polishing should be able to cope effectively with the elevated sizes of the finished products, such as large-calibre space mirrors, laser optical components, etc. [2, 3]. However, the complex geometry of components may restrict polishing tools to access the workpiece surface directly. Therefore, some noncontact polishing methods were developed, such as magnetorheological finishing (MRF), magnetorheological jet polishing (MJP) and abrasive jet polishing (AJP) [4].

As a non-traditional type of optical parts processing method, MRF was investigated by Kordonski and Golini [5] in consideration of electromagnetics, fluid dynamics and analytical chemistry. Such a method provides a small gap between the workpiece surface and the polishing pad. When the magnetorheological polishing liquid passes the small gap, the gradient magnetic flux makes a rheological liquid stiffer or harder, similar to the Bingham medium with high viscosity. When a rheological fluid with a high viscosity enters a small gap, the area in contact with the surface of the workpiece generates a large shear force, so that the material on the surface of the workpiece is removed [6]. Kordonski and Golini in 2002 [7] further studied the applications of magnetorheological effect in high precision finishing and designed a special means for fluid removal from the polishing wheel and returning to the delivery system.

Bombard and de Vicente [8] invested the tribological performance of magnetorheological (MR) fluids in pure sliding soft-elastohydrodynamic lubrication (EHL) steel/polytetrafluoroethylene (PTFE) point contacts. The hardness of the magnetorheological fluid involved in polishing can be controlled by the magnetic field, and the material removal method is changed to the shearing effect of the abrasive flow tangential direction, with almost no subsurface damage, and the polishing efficiency is greatly improved compared with ion beam processing. Therefore, the removal rate is controllable. However, the friction coefficient of MRF fluid depends strongly on the viscosity of the lubricant oil. The research shows the configuration of MRF liquids is complex because there are many parameters should be considered such as abrasive diameters, the magnetic field intensity, the magnetic flux directions and the magnetic pole shape. Ghosh et al. [9] invested the surface roughness and residual stress in MRF, the wheel based magnetorheological finishing (MRF) process is used to attain nano-level surface roughness of oxygen-free high conductivity (OFHC) copper. As polishing tools do not contact to the workpiece in MRF, the wear of the polishing tools and temperature of the polishing area is stable, which improve the polishing accuracy. Nevertheless, the system of MRF is complex and the polishing cost is high. It is necessary to configure different magnetorheological fluids according to different workpiece materials [10].

Childs et al. [11] researched the material removal mechanism of the magnetic fluid grinding. The high removal rate occurs when large sliding velocities occurs between the balls (workpiece) and drive shaft. A kinematic theory was developed to calculate sliding velocities and was applied to derive the material wear coefficient. The material removal rates were verified by the experiments. It should be noted that magnetic fluid grinding (MFG) is not same as MRF, but the abrasion interactions identified within a magnetic field may have referential significance.

Abrasive jet polishing (AJP) technology, like MRF, does not require a polishing nozzle pad direct contacts with the workpiece, so no thermal deformation occurs. It also takes the advantage of fluid conformability, so the abrasive flow configuration is simple, and the processing cost is lower than MRF. Similar to other polishing, it can polish almost all materials and geometric shapes, especially in the precision polishing of hard and brittle materials. These characteristics make AJP one of the most ideal precision processing technologies nowadays.

During the studying on the smoothing process of the rough surface of diamond thin-films in 1992, Hashish and Bothell [12] found that the workpieces were cut or micro-cut more effectively by ejecting abrasive particles along the tangential direction rather than with a small incidence angle, which is

the angle between the injection direction of the jet and the normal direction to the surface. However, the applied pressure and velocities (over 150 m/s) is comparably high for most polishing application. Accordingly, in 1998, Fahnle et al. [13] adopted a low-pressure micro-abrasive jet with a nozzle in a controllable way to impose the impacts on the workpieces. The material removal process of AJP was further analysed in 1999 by Fahnle and van Brug [14], resulting significant improvement in the surface quality of the complex aspherical optical component. It was found that the geometry precision of the polishing area depends on the nozzle diameter, but nozzles of tiny size are easily clogged or worn out.

An abrasive jet begins to diverge and lose coherence momentum when it exits from the nozzle. This is caused by a combination of the sudden drop of pressure and surface tension in both tangential and normal directions with aerodynamic interference [15]. Since the workpiece surface has a certain distance from the nozzle, the divergence of jet beam may diminish the stability of the flow and consequently, the polishing spot reduces the accuracy of the workpiece shape. Furthermore, the large impact angles of the jet may cause the normal impact on the surface of the workpiece, which could have negative effects on the surface quality, such as poor surface roughness and subsurface fracture. Similar experiments were conducted by Booij et al. in 2002 [16], who depicted the theoretical dependence of the material removal rate on various key parameters of AJP processes. In 2004, they [17] concluded that improved surface shapes could be achieved by adjusting the movement of the nozzle trails. In Messelink et al.'s research [18], a micro-abrasive jet with a sub-aperture shape correction was used to perform polishing machining on aspherical surface. By mixing a well-controlled amount of gas into the abrasive flow, a large processing depth removal from nanometres to micrometres was acquired. Of these investigations, the negative effect of the divergence of jet beam and the normal impact were not mentioned. Matsumura et al. [19] studied the stagnation effect of abrasive water jet during polishing glass microgroove surface, where the vertical flow from the jet nozzle was changed to horizontal flow around the stagnation area. When the abrasive jet flow impact to a flat surface, brittle fracture could occur. Because the stagnation area is very small, the horizontal flow helps to remove the material without brittle fracture, crack-free surfaces of glass workpiece were generated.

Kalirasu [20] proposed a hybrid objective function to optimize the control parameters of abrasive water jet machining (AWJM) of jute/polyester composite using a cost-effective Multi Objective Optimization by Ratio Analysis named as MOORA model. The feed rate is the most obvious factor, at the same time, the standoff distance has some influence to machining results. Wang et al. [21] proposed a predictive model of the machined surface topography in the AAJP process research, where the standoff distance and jet impact angle were set as the key input machining parameters, and the divergence of jets and the impact damages of the abrasive jet were considered as outputs of the model.

Magnetorheological jet polishing (MJP) is a combination of AJP and MRP [22]. It uses low-viscosity magnetorheological fluid to generate magnetorheological effects under the action of an external magnetic field to form a collimated hardened jet beam to impact the surface of the workpiece [23]. MJP corrects the problem of jet beam divergence during processing. Material is removed by the high-speed impact and shear action of abrasive particles, but mid-spatial frequency (MSF) errors should be considered in MJP with a simple vertical jetting model. Wang et al. [24] proposed a weighted iterative algorithm to restrain the MSF errors.Yang et al. [25] built a more comprehensive model for MJP removal mechanisms and applied it in reducing edge effects in surface polishing of thin rolled edges with a reduction of profile RMS from 10.5 nm to 1.4 nm. However, like traditional AJP, the MJP jet beam is not parallel to the workpiece surface, which causes large normal impact, inducing impact damage on the surface or subsurface of the workpiece. Furthermore, the preparation of the magnetic abrasive particle flow is complicated and expensive, similar to MRF.

Polishing complex surface of hard and brittle materials parts by abrasive jet is feasible as mentioned above; however, some problems remain to be overcome, such as the nozzle wear, the divergent of jets, and the jet impact damages. In this paper, a constrained abrasive jet polishing (CAJP) with a novel nozzle was developed, where a powerful constrained abrasive jet was formed and directed by a head shroud around polishing tool. In this way, the abrasive jet flows in parallel to the workpiece surface. Shifting along the workpiece surface, the abrasive jet was constrained and exiting the slit gap, making almost all abrasives acting force along the workpiece surface transformed into tangential shearing stress. As a result, such a polishing process mainly depends on the shearing and scratching on the surface rather than normal mechanical impact, which not only decreases of impact damages, but also enhances polishing precision and efficiency. Moreover, a slender nozzle is no longer a necessity to form the jet, and the cost could be great reduced by the recycling of the abrasive fluid, which is also beneficial by reducing environmental pollution. Compared to AJP and MJP, CAJP gives minimum normal jet impact.

2 The design of the novel CAJP nozzle

In order to assure the jet abrasives flow along the workpiece surface, a CAJP nozzle head is designed with a structure that contains a core and a shroud as sketched in Fig. 1, where α is the inject angle and F_{motor} is the nozzle driving motor holding force for balancing the hydraulic pressure reaction, which depends on nozzle orifice setting. Before polishing, the polishing tool head was pressed on the workpiece surface

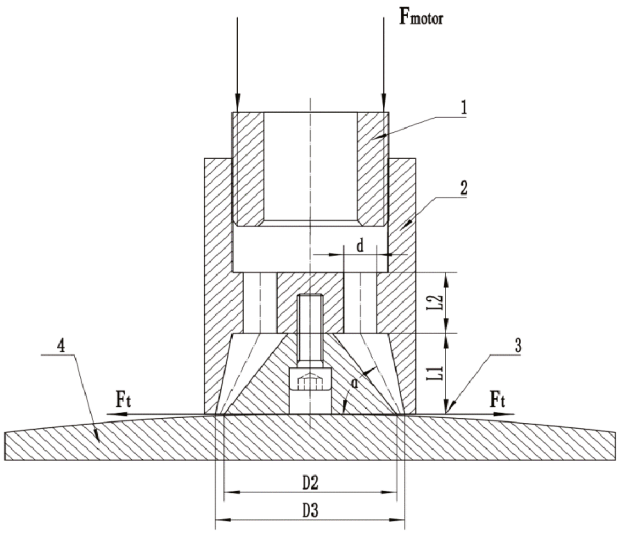

1 Nozzle, 2 shroud, 3 jet, 4 workpiece

Fig. 1 Polishing schematic of the abrasive jet with specified nozzle

with a pre-set force for a selected nozzle slit gap. When the abrasive flow is push out from nozzle, the pressure under the nozzle tool will overcome the preload force and lift the tool head to allow abrasive jets formed along the nozzle slit gap. Through the polishing tool head, the abrasive flow changes its direction to form a tangential jet under the restraint shroud. Precision polishing could be controlled by adjusting the polishing dwelling time and the volume of the abrasive flow.

The nozzle head shroud is designed as a replaceable module and is capable to match up with different workpiece shapes. In order to achieve a long-lasting equable "contact" between the CAJP tool head and workpiece surface, wear-resistant elastic materials, such as nylon and polyurethane, were chosen for the tool head shroud. Figure 1 shows the dimensions of polishing nozzle head design, which was also used as a model for the simulation analysis of nozzle performance. The outer diameter of the tool head is 36 mm, the inner diameter of the inlet section is 28 mm, the inner diameter of the annular outlet $D_2 = 28$ mm and the outer diameter of the annular outlet $D_3 = 32$ mm. A funnel length $L_1 = 16$ mm is designed at the exit section, so that an abrasive flow can be fully developed when the jet flowing from the shunt section ($L_2 = 12$ mm) to the exit section. The polishing tool has 8 separated channel holes in the middle part. The diameters of these channel holes are $d = 6$ mm. Therefore, the total flow cross section area is present in Eq. (1).

$$A_M = 8\pi\left(\frac{d}{2}\right)^2 = 72\pi\ (mm^2) \tag{1}$$

To ensure the continuity for a stable flow in the tool head, the area of the annular section A_{Out} should be less than the sum of the base area of eight cylinders A_M. According to the dimension in the design,

$$A_{Out} = \pi\left(\frac{D_3}{2}\right)^2 - \pi\left(\frac{D_2}{2}\right)^2 = 60\ \pi\ (mm^2) \tag{2}$$

So, the inlet cross section is larger than the outlet one comfortably.

The gap between the nozzle shroud and the surface of the workpiece is one of the key parameters of CAJP. In order to control the polishing gap during the process, it is necessary to know the relationship between the push force of the motor (F_{motor}) and the gap x between nozzle and workpiece as presented in Eq. (3), which could be determined through experiments.

$$F_{motor} + f_{friction} + G = A_{Out} P_{fluid} \tag{3}$$

As the friction coefficient of linear bearings used in the polishing tool is small, the friction force ($f_{friction}$) can be ignored. The gravity of the polish tool (G) measured by the experiment, which is 6.6 N. As shown in Table 1, the inlet fluid pressure (P_{fluid}) associated with different gaps were measured through experiments.

Considering the limited power of the abrasive flow pump, an exponential function was chosen for modelling the relation between fluid pressure P_{fluid} and orifice gap x.

$$P_{fluid} = 0.4915\ e^{-0.679x} \tag{4}$$

The determination coefficient R^2 is 0.86, which means the variation could be high between the fluid pressure and orifice gap. Therefore, the equation could only serve as an initial setting reference to avoid significant deflection error. The motor driving force is therefore presented as Eq. (5). The actual pressure and force should be measured in situ.

$$F_{motor} = 60\pi\left(0.3235e^{-0.204x}\right) - 6.6 \tag{5}$$

3 Simulation of abrasive flow in the nozzle and surround polishing area

3.1 Abrasive flow modelling

In order to gain an insight of the CAJP process, the investigation focuses on the abrasive jet flow dynamic performance. During CAJP process, the abrasive flow passes through the shrouded nozzle forming a plane jet, which is an

Table 1 The relationship between gap and fluid pressure

Gap x(mm)	P_{fluid}(MPa)
1.0	0.2756
1.25	0.2391
1.5	0.1506
1.75	0.1337
2.0	0.1119
2.5	0.1069

incompressible low viscosity two-phase flow with 15% scattered floating abrasive particles. The relevant physical parameters were determined by experiments. The flow liquid density of the abrasive flow ρ_l is 1134.8 kg/m^3 and the density of the abrasive ρ_s is 3170 kg/m^3, so the density ρ of the two-phase abrasive flow is 1440 kg/m^3. The viscosity μ of the abrasive flow is 2.355 $mPa{\cdot}s$. To consider the flow status in the CAJP system, the Reynolds number calculation is shown in Table 2.

In Table 2, Re_0 is the Reynolds number, v_0 is the average speed of the jet at the exit slit. The d_H is the hydraulic diameter. c is the perimeter of the cross-section of the fluid contact to solid region. The internal flow of the abrasive jet usually is a turbulent jet according to the engineer experience, when $Re_0 > 3500$ [26].

In order to make the Reynolds equations solvable, the unknown correlation elements in the Reynolds equations or in the transport equations of the turbulent characteristics were expressed in term of the low order correlation or the time average. In fact, the jet flow in the near wall region is a kind of low Reynolds number turbulence as the effects of the wall and the viscous of the flow, the various scales of turbulence and the characteristics of transport and dissipation are different from the fully developed turbulence, that shows a fairly inhomogeneous and anisotropic. So the calculation accuracy of the standard $k-\varepsilon$ model is not good enough in the near wall region. The *SST* (Menter's Shear Stress Transport) turbulence model [27] which use a low Reynolds number $k-\omega$ mode in near wall region was reasonably adopted. The standard *k-ε* model only applied at the end of the external flow zone and the free shear layers. A smooth transformation of the mixed function between these two models was established [28, 29].

The mathematical expressions for SST turbulence models are as follows.

$$\frac{D(\rho k)}{Dt} = \tau_{ij}\frac{\partial u_i}{\partial x_j} - \beta^* \rho k\omega + \frac{\partial}{\partial x_j}\left(\Gamma_k \frac{\partial k}{\partial x_j}\right) \tag{6}$$

$$\begin{aligned}\frac{D(\rho\omega)}{Dt} = {} & \frac{\gamma}{\nu_t}\tau_{ij}\frac{\partial u_i}{\partial x_j} - \beta\rho\omega^2 + \frac{\partial}{\partial x_j}\left(\Gamma_\omega \frac{\partial \omega}{\partial x_j}\right) \\ & + 2\rho(1-F_1)\sigma_{\omega,2}\frac{1}{\omega}\frac{\partial k}{\partial x_j}\frac{\partial \omega}{\partial x_j}\end{aligned} \tag{7}$$

The expression of the shear stress τ_{ij} is as follows.

Table 2 Reynolds number calculation

Parameters	Formula	Results
c	$c = \frac{1}{2}\pi(D_2 + D_3)$	30π
d_H	$d_H = 4\frac{A_{Qw}}{c}$	8 mm
ν	$\nu = \frac{\mu}{\rho}$	$1.635 \times 10^{-6} m^2/s$
Re_0	$Re_0 = \frac{v_0 d_H}{\nu}$	39,148 ~ 53,823, when $v_0 = 8 \sim 11$ m/s

$$\tau_{ij} = \mu_t\left(\frac{\partial u_i}{\partial x_j} + \frac{\partial u_j}{\partial x_i} - \frac{2}{3}\frac{\partial u_k}{\partial x_k}\delta_{ij}\right) - \frac{2}{3}\rho k\delta_{ij}. \tag{8}$$

In formula (8), δ_{ij} is the Kronecker function [30].

$$\delta_{ij} = \begin{cases} 1 & i = j \\ 0 & i \neq j, \end{cases} \tag{9}$$

In formulas (6) and (7), $\tau_{ij}\frac{u_i}{x_j}$ can be expressed as,

$$\tau_{ij}\frac{\partial u_i}{\partial x_j} = \mu_t\left[s_{ij}^2 - \frac{2}{3}\left(\frac{\partial u_k}{\partial x_k}\right)^2\right] - \frac{2}{3}\rho k\frac{\partial u_k}{\partial x_k} \tag{10}$$

In formula (10),

$$s_{ij} = \frac{\partial u_i}{\partial x_j} + \frac{\partial u_j}{\partial x_i} \tag{11}$$

In formulas (6) and (7), Γ_k and Γ_ω represent the effective diffusion term of the k and ω respectively, $\beta^\star \rho k\omega$ and $\beta\rho\omega^2$ represents the divergence term respectively. The last item of formula (7) represents an orthogonal divergence term.

The equations of the effective diffusion term,

$$\Gamma_\omega = \mu + \sigma_\omega \mu_t, \tag{12}$$

$$\Gamma_k = \mu + \sigma_k \mu_t, \tag{13}$$

$$\sigma_k = F_1\sigma_{k,1} + (1-F_1)\sigma_{k,2}, \tag{14}$$

$$\sigma_\omega = F_1\sigma_{\omega,1} + (1-F_1)\sigma_{\omega,2}. \tag{15}$$

The switching function F_1 is expressed as follows,

$$F_1 = \tanh\left(\theta_1^4\right) \tag{16}$$

$$\theta_1 = \min\left[C, \frac{4\sigma_{\omega,2}\rho k}{D^+ y^2}\right] \tag{17}$$

$$C = \max\left(\frac{\sqrt{k}}{0.09\omega y}, \frac{500\nu}{y^2\omega}\right) \tag{18}$$

$$D^+ = \max\left(\frac{2\rho\sigma_{\omega,2}}{\omega}\frac{k}{x_j}\frac{\omega}{x_j}, 10^{-10}\right) \tag{19}$$

In formulas (17) and (18), y is the shortest distance from the current point to the physical plane, D^+ is the positive portion of the orthogonal divergence term in Eq. (7).

The function expression of the SST turbulence model, $k-\omega$ turbulence model and standard $k-\varepsilon$ turbulence model are ϕ, ϕ_1 and ϕ_2, respectively, the function relation between the three is as follow,

Table 3 Constant value in *SST* turbulence model

$\sigma_{k,1} = 0.85$	$\sigma_{k,2} = 1.0$	$\sigma_{\omega,1} = 0.5$
$\sigma_{\omega,2} = 0.856$	$\alpha_1 = 0.31$	$\beta^* = 0.09$
$\kappa = 0.41$	$\beta_{i,1} = 0.075$	$\beta_{i,2} = 0.0828$
$\gamma_1 = 5/9$	$\nu_t = k/\omega$	

$$\phi = F_1\phi_1 + (1 - F_1)\phi_2 \tag{20}$$

When ϕ_1 approaching to 0, F_1 is close to 0 too. In this investigation, the turbulence model applied in this zone is the standard $k-\varepsilon$ model [31].

$$\gamma_1 = \beta_{i,1}/\beta^* - \sigma_{\omega,1}\kappa^2/\sqrt{\beta^*} \tag{21}$$

$$\gamma_2 = \beta_{i,2}/\beta^* - \sigma_{\omega,2}\kappa^2/\sqrt{\beta^*} \tag{22}$$

The vortex coefficient is defined as follows,

$$\nu_t = \frac{\alpha_1 k}{\max(\alpha_1\omega, F_2)} \tag{23}$$

The formulation of F_2 and θ_2 are expressed as follows.

$$F_2 = \tanh(\theta_2^2) \tag{24}$$

$$\theta_2 = \max\left(\frac{2\sqrt{k}}{0.09\omega y}, \frac{500\nu}{y^2\omega}\right) \tag{25}$$

When $F_1 = 1, \theta = \theta_1$ this is $k-\omega$ turbulence model. The constant values in *SST* are shown in the Table 3.

3.2 Abrasive flow inside the nozzle

In order to fully understand the constrained abrasive jet flow, the internal flow of the nozzle tool was first analysed to estimate the velocity and pressure of the internal flow at the exit orifice gap, which will then be used as the initial parameters of the abrasive jet in polishing zone. The performance of abrasive jet was simulated thereafter to illustrate the material removal mechanism of the CAJP based on the fluid mechanics.

A finite element method was adopted and the element meshes of the internal flow are set up using ICEM CFD software as shown in Fig. 2a, where only one eighth of the flow field in the nozzle was taken into account, because the nozzle head was an axisymmetric structure. The total simulation detection line length of flow channel in Fig. 2b is 47 mm. The max mesh size is 0.25 mm and the min mesh size is 0.1 mm. The minimum volume of mesh isn't a negative that accord with the criteria for the effective mesh in finite element analysis. The hexahedral meshing was adopted and the top-down "sculpture" grid division method was used, multiple topological blocks of the structure grid can generate. The high quality "O", "C", "L" - shaped hexahedral meshes were applied and the local grids were refined in the nozzle part. The total number of grids is 57915. The split surfaces of both sides of the simulation model sections were set as periodic symmetric boundary. A detection line, as indicated in Fig. 2b, was set in the middle of abrasive flow for the pressure and velocity reading during simulation. In this way, the variation of pressure and speed of the flow can be illustrated and studied. For the abrasive flow simulation, the initial velocity at the inlet of the nozzle was set as 6 m/s. The outlet outflow was determined based on the continuity of the flows in the nozzle channels.

The pressure distribution and velocity values in the nozzle channels are shown in Fig. 3. The pressure and speed varying along with the flow detection line are extracted in Fig. 3c. Simulation results indicated that the diversion column will increase the abrasive flow speed and reduce the abrasive flow pressure. It was observed that the speed of abrasive flow in the slit exit increased to approximately

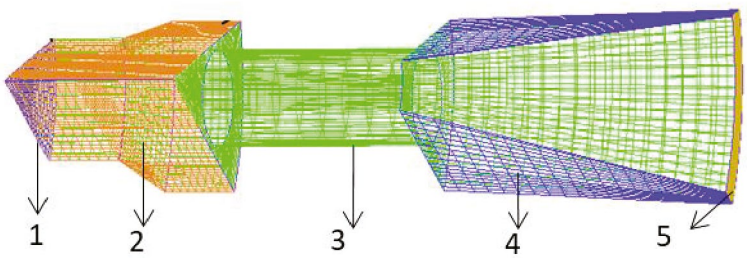

1. Inlet; 2,4. Periodic symmetric boundary; 3 Division columns; 5 Outlet

(a) Meshes of the internal abrasive flow

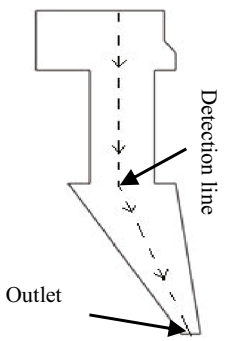

(b) Position of detection line

Fig. 2 Simulation model of the internal abrasive flow

11 m/s in the direction along the tangent of the bottom surface of the polishing tool.

By lifting the nozzle from workpiece surface to adjust the nozzle slit gap, the velocity of the outflow jet can be controlled. Table 4 shows simulated variation of abrasive flow velocity at the outlet of the nozzle, they decrease with the increase of the exit slit height.

3.3 The simulation of surface polishing jet

The CAJP abrasive jet can be considered as a kind of planar jet flow parallel to the workpiece surface, which was modelled and meshed as shown in Fig. 4. The flow status at the outlet of the nozzle was set as the inlet of the slit planar jet simulation model. With the analogue of slit jet from the centre of nozzle, the lengths of the main jet segment in radius direction is less than 15 mm and the width is around 10 mm. The nozzle centre was aligned to the coordinate origin, so the length of the simulation model was set up to 30 mm covering the abrasive flow jet outside of the nozzle.

By taking the simulation results of nozzle internal abrasive flow, the simulation of slit planar jet adopted the initial inlet speed of was set as 8 m/s, 9 m/s, 11 m/s and 15 m/s respectively according to the slit gaps as shown in Table 4.

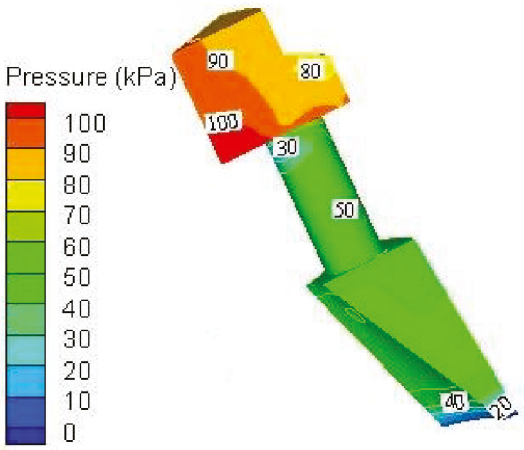

(a) Pressure distribution of internal flow

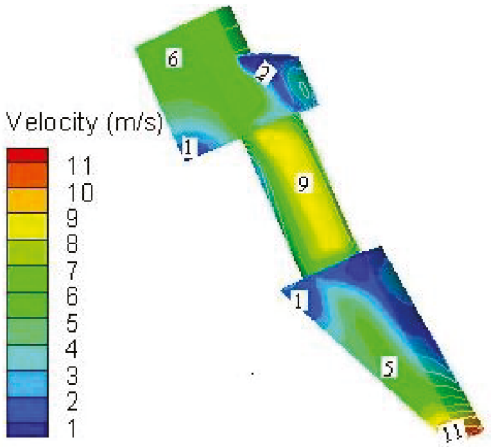

(b) Velocity vectors of internal flow

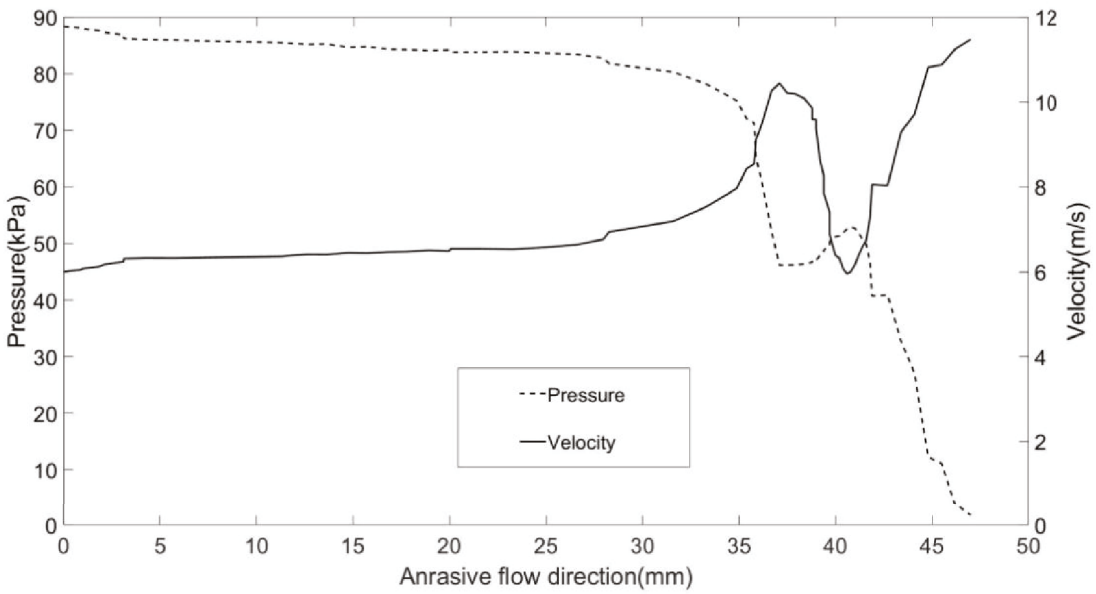

(c) Pressure and speed change along the detection line illustrated in Fig. 2(b)

Fig. 3 Simulation results of the internal abrasive flow

Table 4 Out pressure and velocity of vary exit slit

Exit slit (mm)	Nozzle outlet velocity (m/s)	Nozzle inlet pressure (kPa)
1	15	90
1.5	11	50
2	9	30
2.5	8	15

The simulated pressure distribution of the slit planar jet is presented in Fig. 5, where the pressure under the nozzle shroud increases significantly when slit gap decreases. When the nozzle slit gap decreases down to 1 mm, the pressure variation under nozzle shroud becomes obviously in both horizontal and vertical directions. The pressure changes little when the jet exits the nozzle more than 5 mm in distance (i.e., radial X coordinates > 20 mm in Fig. 4). The orientation of the nozzle exit slit decreases the normal pressure of the abrasive flow on workpiece surface, so the active polishing region of the jet has a stable tangential shear stress. The pressure under the nozzle central block appears negative forming a circular flow; however, when the slit gap decreases (around 1 mm), the pressure increases to near zero level.

Figure 6 shows the simulation results of abrasive jet velocity in the slit planar jet flow. It can be seen that CAJP nozzle can change abrasive flow velocity direction quickly to parallel to the workpiece surface, so as to limit the impact to reduce potential damage to the workpiece. The streamlines of the slit jet show that abrasives would move horizontally in the slit gap region under the should (CAJP nozzle radial position X = 16 ~ 18 mm). This is a beneficial process feature for polishing. The flow speed increases significantly in the slit channel, but reduces afterward to a stable value along the workpiece surface. It is interesting to see that the abrasive flow on the workpiece surface outside of nozzle shroud actually moves backward towards nozzle. Such a backward flow may have a deleterious effect to the polishing quality, which will be discussed later. There exists a point around X = 18 ~ 20 mm where flow speed on workpiece surface is near zero. If the nozzle slit gap is larger than 2.5 mm (include 2.5 mm), the abrasive jet velocity near workpiece surface decrease drastically, which no longer polishing effectively.

In order to identify the real material removal performance in the CAJP process, both the profiles of abrasive flow speed and pressure along the workpiece surface should be considered comprehensively as shown in Fig. 7a, b, where the points A, B, C, D, E and F are selected to be compared with experimental polishing tests. The speed and the pressure values are taken from the detection line that is 0.2 mm above the surface.

As the nozzle outlet position locates on X = 15 mm, the surface of workpiece at the position X greater than 15 mm is the subjects of polishing area. In this region, the velocity vector of the abrasive flow increases rapidly firstly and then decreases close to 0 for each fixed nozzle lifting height. If the lifting height of the polishing head decreases, the maximum speed value in the polishing region will increases. Similarly, the flow pressure increases rapidly and decrease gradually along the radial position in X direction. If nozzle lifting height decreases, the maximum pressure in the slit polishing region will increase, and the polishing region increased too. As the part of the x-coordinates less than 15 mm isn't work region, so the changing trend of the velocity vector in this part does not contribute material removal much.

Materials removal in an abrasion process could be calculated based on Preston formula [32, 33], where the abrasion

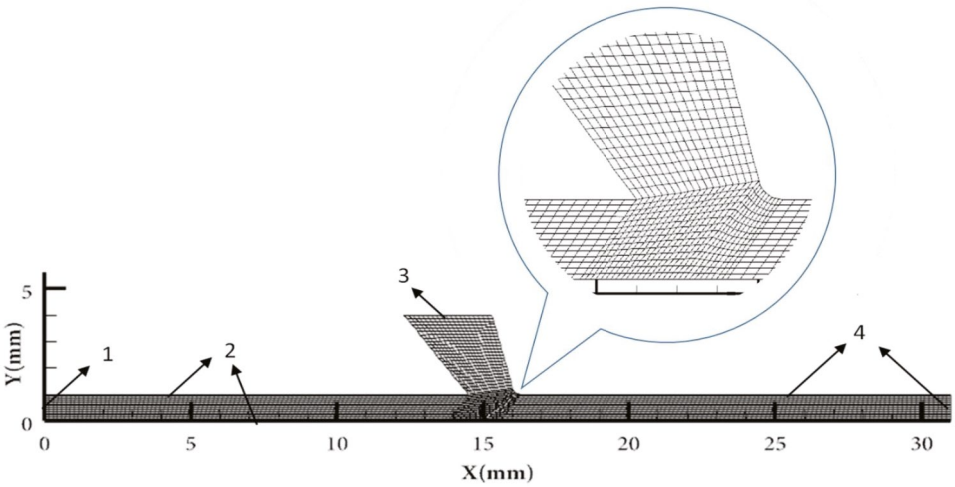

Fig. 4 Simulation model and meshes of the jet in polishing zone

1 Periodic symmetric boundary; 2 Wall; 3 Inlet; 4 Outlet

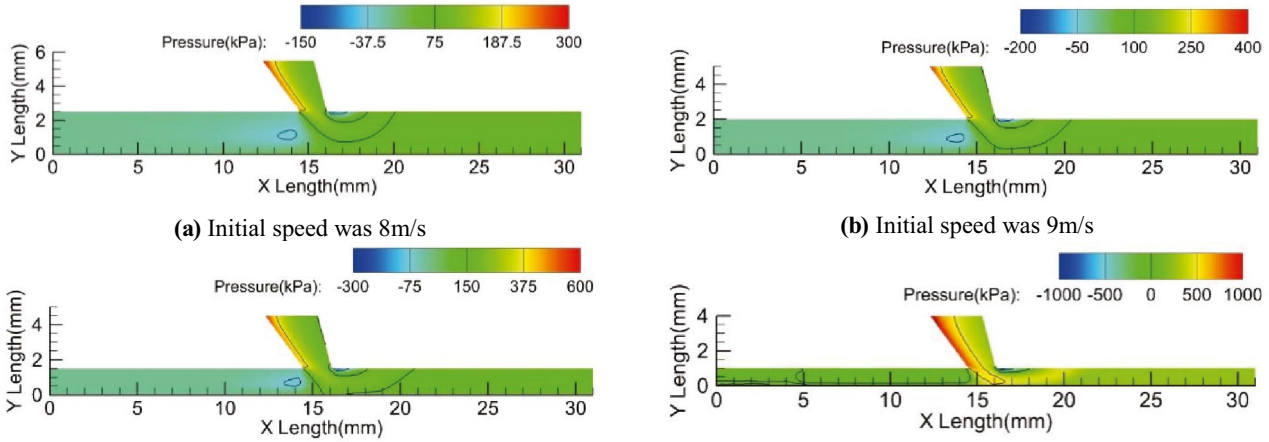

(a) Initial speed was 8m/s

(b) Initial speed was 9m/s

(c) Initial speed was 11m/s

(d) Initial speed was 15m/s

Fig. 5 Pressure distribution of abrasive jet in polishing zone

material removal rate (MRR) is positively correlated with the speed and pressure.

$$MRR(x) = \frac{k_p}{T}\int_0^T p(x)v(x)dt \tag{26}$$

where T is the abrasion process time, $v(x)$ is the instantaneous speed of the jet on the surface of the workpiece irrespective the flow direction, $p(x)$ is the instantaneous pressure of the jet on the surface of the workpiece. k_p is the coefficient of the Preston formula, which is expressed as

$$k_p = k_1 k_2 k_3 \tag{27}$$

k_1 considers the injection angle of the jet, which should be determined through the experiment. k_2 considers the affection of the hardness of the abrasive, which can be expressed as

$$k_2 = \frac{H_p}{H_f} \tag{28}$$

H_f is the hardness of the workpiece *and* H_p is the hardness of the abrasive. For the case under the consideration (K9 glass H_f is 610 kg/mm^2 and alumina H_p is 2000 kg/mm^2), the k_2 *is 3.28.*

The parameter k_3 considers the effect of the abrasive grit concentration and the size of the abrasive grits, which should be determined through the experiment too. Considering a case where $k_p = 1.82 \times 10^{-11}$MPa^{-1}, the variation of polishing removal rate due to the change of nozzle slit gap is presented in Fig. 7c. It can be seen that the effective polishing region is around position X = 15–20 mm. The smaller slit gap, the higher the removal rate.

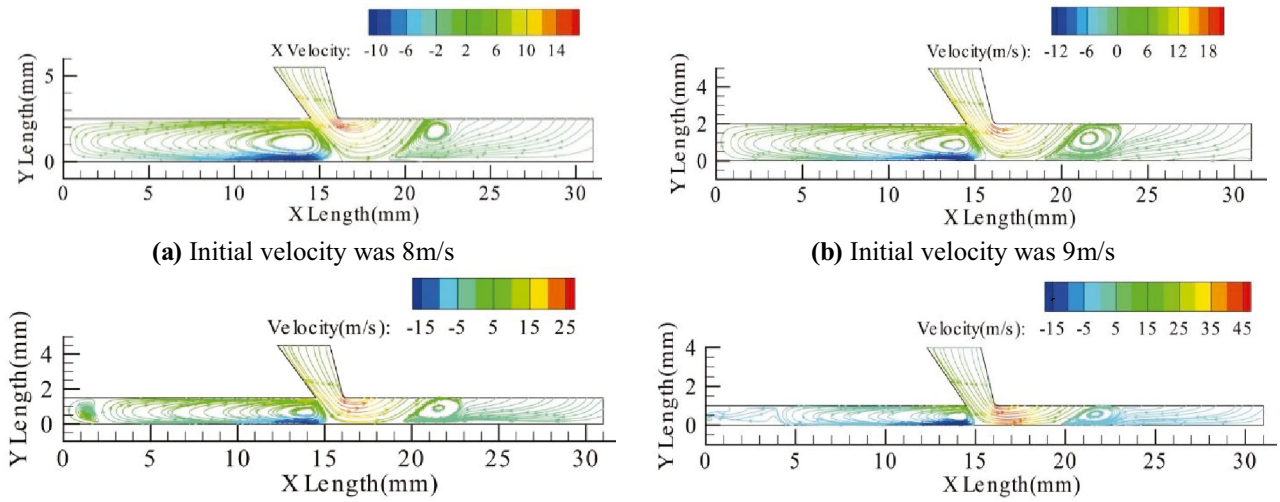

(a) Initial velocity was 8m/s

(b) Initial velocity was 9m/s

(c) Initial velocity was 11m/s

(d) Initial velocity was 15m/s

Fig. 6 The speed streamline of the abrasive jet flow in polishing zone

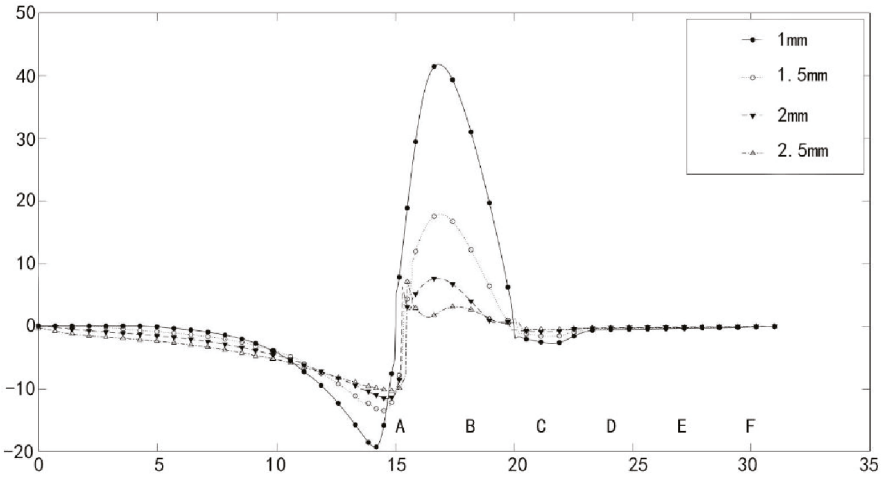

(a) Variation of average speed along radial direction

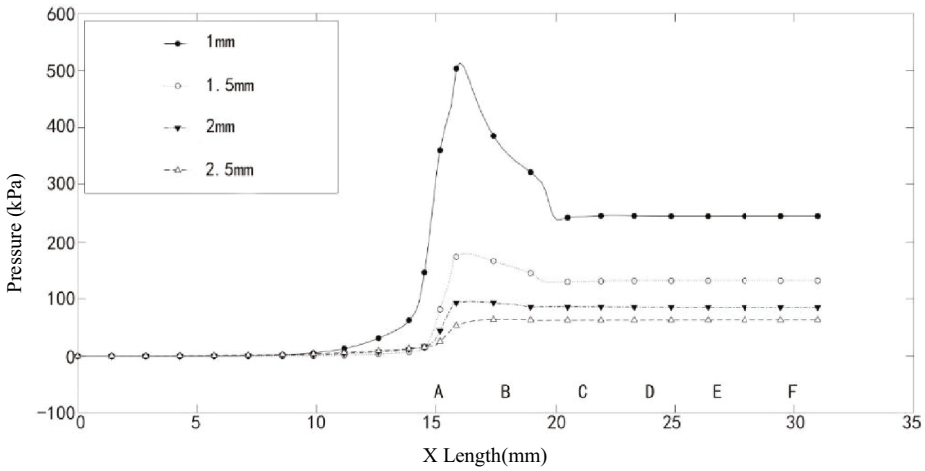

(b) Variation of average pressure along radial direction

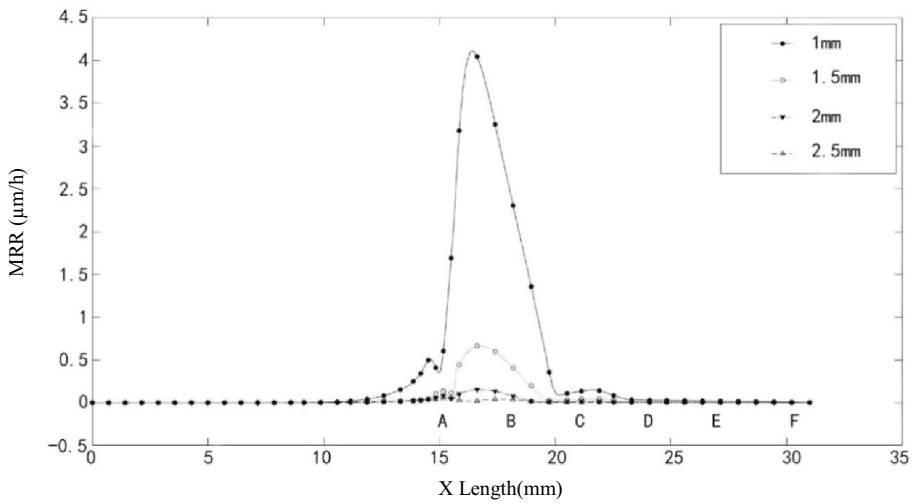

(c) Material removal rate along radial direction calculated based on Preston model

Fig. 7 Comparison of CAJP performance simulation results under different nozzle slit gaps

Table 5 Material properties of K9 Glass [34]

Parameters	Value
Density (kg/m^3)	2520
Knoop hardness H_K (kg/mm^2)	6100
Vickers hardness Hv (N/mm^2)	7120
Young's Elastic modulus (Gpa)	82
Poisson Ratio	0.21
Shear modulus (Gpa)	30.4
Fracture toughness (Mpa·m$^{1/2}$)	2.63
Tensile strength (Gpa)	0.15
Hug elastic limit (GPa)	5.95

4 Experimental investigation of CAJP

In order to evaluate the CAJP nozzle performance, a set of polishing experiments were performed on K9 optical glass, a typical hard and brittle material. The physical and chemical properties of K9 optic glass is shown in Table 5. Figure 8 illustrates a polishing experiment platform that was built with the CAJP nozzle mounted on a high-precision Motorman HP 20 robot arm. The polishing path was manipulated by the robot arm according to the requirement. The workpiece was fixed with a pan on a stationary rotational table, and the abrasive jet ejected from the nozzle along the redial direction along the workpiece surface. Therefore, the actual abrasive flow trajectories on the workpiece surface are the combination of the motions mentioned above. In the experiment, the sample on the table keeps stationary. Six checking points on the sample were defined as A to F in Fig. 7 in corresponding to polishing path in radial direction; and these point positions on the sample surface are illustrated in Fig. 9. The surface conditions at these checking points were examined by Taylor Hobson contours & roughness instrument (Form Talysurf i-Series 1) before and after polishing, so that the experimental results can be compared with simulation results. The measurement scope of Form Talysurf i-Series is 5 mm and the resolution is 0.1 nm. The first check point A is set in the middle of the exit section of nozzle channel and the other checking points were arranged with an interval of 3 mm along the nozzle radial direction. The polishing head was positioned and controlled by the linear stepping motor to provide required lifting gaps as defined in Table 1. The key processing parameters are shown in Table 6 and the fluid of used for the abrasive jet was de-ionized water. After processing for a set of defined polishing period, the material removal and surface roughness at each selected point was measured and recorded as shown in Fig. 10.

Fig. 9 Checking points on the sample

As shown in Fig. 10a, the material removal volume at different surface position varies with the polishing time and the distance from the nozzle centre. After one hour polishing,

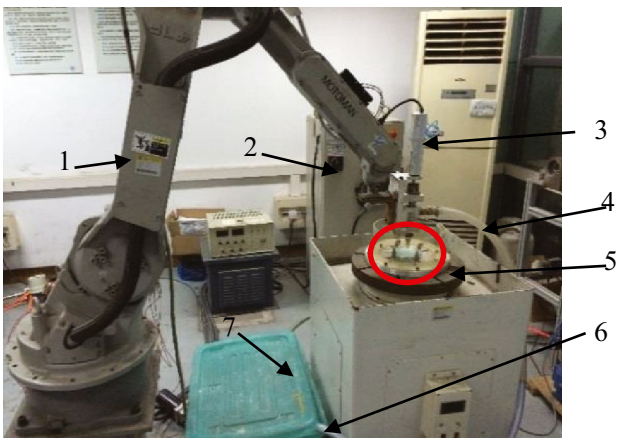

(a) Apparatus setup for AJP process

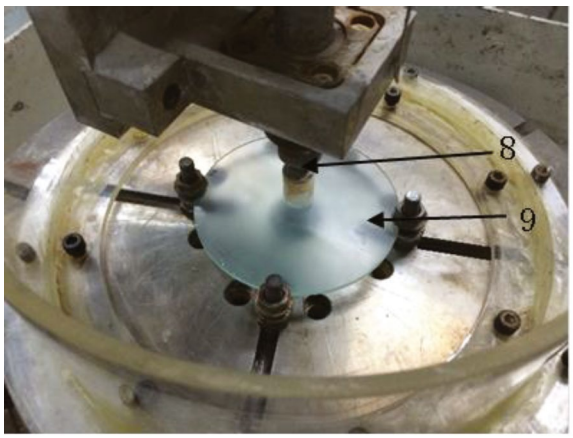

(b) Enlarged local view of process platform

Fig. 8 CAJP experiment setup

Table 6 Experimental parameters

Experimental Control factors	Parameter/Value
Abrasive	Alumina
Sample material	K9 glass
Polishing nozzle gap	1 mm
Abrasive size	10 μm
Abrasive concentration	15%
Additives and concentrations	0.1% Zinc nitrate

the maximum material removal appears at the checking point B in the polishing zone, reaching to 3.42 μm. With continuous polishing, the maximum material removal position shifts to point A. After 4-h polishing, the material removal at point A became the largest (up to 8 μm). According to Preston model, the material removal in an abrasion process is the combination actions of abrasive pressure and speed and the maximum material removal would occur at the point where x coordinate is 16.5 mm, in the middle point of A and B. In referring to the simulation results in Fig. 7a, b, the highest pressure at the point where x coordinate is 15.9 mm, near point A, while the highest speed at the point where x coordinate is 16.9 mm, near point B. The results in Fig. 10a confirm the Preston model presents polishing performance fairly well and could serve a general guidance. The shift of the position of maximum material removal in the experiments indicates the pressure and speed of abrasive flow could change along with the polishing time. The influence of such variations needs further investigation.

Compare the simulation results with the experiment results in Fig. 10a, the simulated results in a unit time (one hour) are similar to the abrasion performance at around one-hour polishing. Both simulations and experiments show the lowest MRR of experiment is point D, where x coordinate is 24 mm. Such a point could be considered as the CAJP polishing boundary. The experimental results show that the material removal increases unexpectedly at those positions beyond the boundary D, i.e. E and F, where the simulation could not illustrate such performance. It is interesting to see that material removal at point F reaches 4.68 μm after 1 h polishing, but it does not increase a lot during further polishing. It may attribute to the flow turbulence away from the nozzle polishing zone, though the mechanism is not clear yet. Look at the abrasive flow streamlines in Fig. 6, there is a big vortex reverse flow existing in the area where x coordinate is larger than 20 mm. The big vortex makes the backflow impact on the workpiece surface, which needs further investigation.

The values of surface roughness in the tests are shown in Fig. 10b. The surface roughness at the point A, B and C was improved significantly with the polishing time, especially at point B, the surface roughness decreased from 386 to 268 nm. The results convinced that CAJP can significantly improve surface finish under the shroud cover area and the decrease of surface roughness at point B is the most pronounced. Outside the nozzle shroud ring, the action of surface roughness improvement decreases. At the point D, the surface roughness improvement becomes much weak, only from 390 to 361 nm. Further away from the nozzle, a longer time polishing would lead worse surface finish. At the point E and F, the roughness of the workpiece surface did not improve, instead, it increased significantly when the polishing lasts longer than two hours. This demonstrated the improvement of surface roughness in an abrasive jet polishing is a very complex process that needs further investigation.

The morphologies of sample surfaces before and after 4-h polishing were examined by Keyence VHX-500 microscope as shown in Fig. 11. Further considering the influence

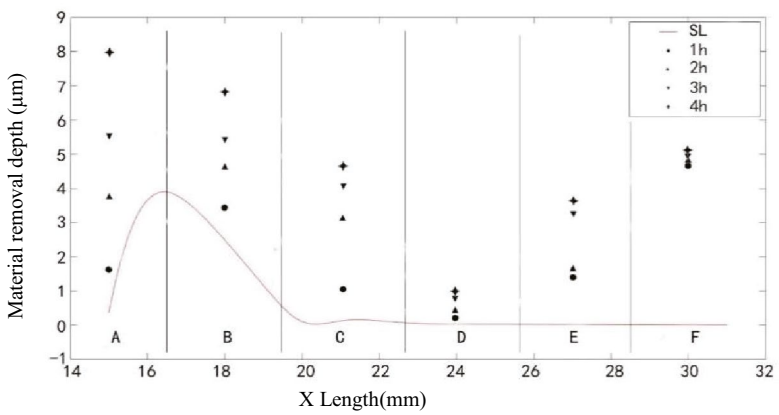

(a) The experimental polishing material removal at different check points compared to the simulation results

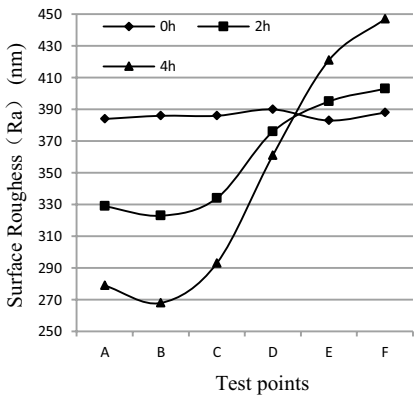

(b) The experimental surface roughness at different test points

Fig. 10 The polishing material removal and surface roughness of CAJP

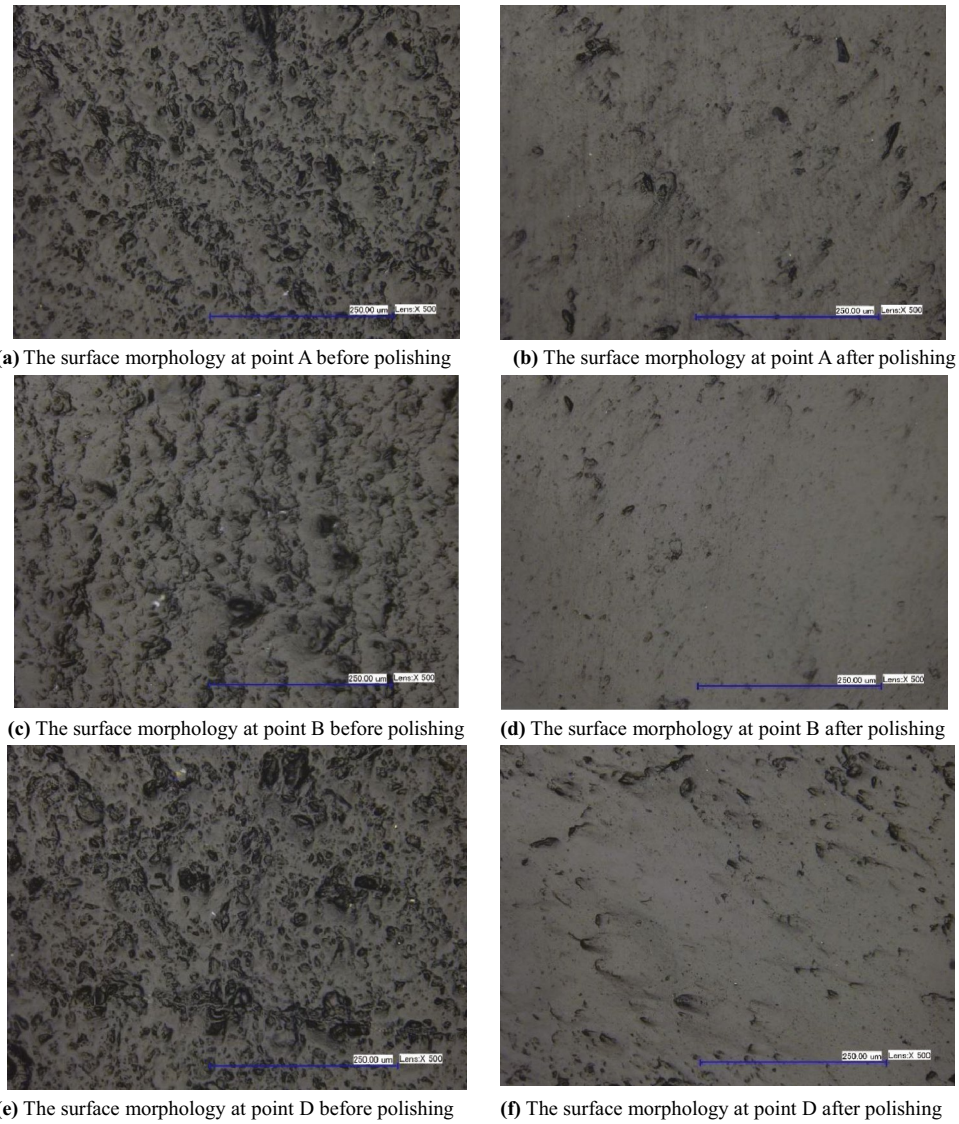

Fig. 11 Surface morphologies of the points in the effective CAJP area before and after 4-h polishing

(a) The surface morphology at point A before polishing

(b) The surface morphology at point A after polishing

(c) The surface morphology at point B before polishing

(d) The surface morphology at point B after polishing

(e) The surface morphology at point D before polishing

(f) The surface morphology at point D after polishing

of material removal on the surface roughness improvement, it needs link to the morphologies of sample surfaces and the position of the polishing. At position A, the middle of the nozzle exit section, the abrasive jet transfers from normal direction to tangential direction, the normal pressure is high, but the flow speed along workpiece surface is relatively low, so the normal impact is the main cause for the material removal. When abrasives move to position B, the speed increases significantly, the material removal in mainly due to horizontal shearing. The simulation results shown that the abrasive jet at the point B is almost parallel to the workpiece surface. This makes the surface roughness improved greatly, the surface roughness decreased considerably. So material removal caused by tangential force is commonly considered as the best way to reduce polishing surface damage. Comprehensive consideration of material removal volume, surface roughness and the polishing performance at the point B is the best. Similar to position B, the horizontal speed at position C is still larger, so it shows good processing results too. The point D is considered as the end of effective polishing range of the jet, where the speed reduced to near zero, so the removal volume is low and the surface roughness improvement is small. Beyond point D, the reverse vortex flow has deleterious effects on the surface roughness. In addition, the normal impact of reversed flow on the polishing surface could increase as indicated in Fig. 7a, which could cause scratches along the radial direction on the surface, resulting in the poorer surface roughness at points E and point F and a higher material removal. It can be seen under the microscope, the material removal is dominated by the shearing and scratching of the workpiece surface rather than the mechanical shock impacts. This is because tangentially aligned nozzle shroud constrained abrasive flow parallel to the polishing surface.

5 Conclusions

With the theoretical analysis and simulation, it has demonstrated the abrasive flow dynamic performance in the constrained abrasive jet nozzle and the working region of the CAJP. The materials removal performance presented by theoretical analysis matches well with the experimental polishing results. A few findings can be summarised as:

1. The simulation of the internal flow shows that the jet speed and pressure increased with the decrease of the slit gap between the bottom surface of the polishing tool head and the surface of the workpiece. In addition, it is noticed that the jet pressure near workpiece surface increased further when slit gap became narrower, which could be beneficial to material removal in CAJP.
2. The simulation results show that the CAJP abrasive flow velocity at the area under nozzle shroud appears parallel to the workpiece, which helps for surface quality improvement. Compared to a traditional AJP, it not only solved the divergence of the jet beam, but also made the abrasive particles move along the workpiece surface. The constraint shroud strengthened the shearing action of abrasives in polishing and reduced the normal direction impact, which depressed potential occurrence of surface defects.
3. The material removal volume and the surface roughness of polished surface depend on the pressure and speed of abrasive jet. The experimental results illustrated that the polishing function of the CAJP with the novel nozzle shroud mainly relied on the shearing actions of the high-speed jet and the effective polishing distance of the jet is determined by shroud cover area. It is noticed that reversed abrasive jet flows could appear outside of the nozzle shroud ring, that may cause deleterious effects to polished surface if the polishing a very long time. Further investigation is required to understand such flow reversion and limit its influence.
4. It has shown that Preston model provides a good indication of material removal in an abrasion process, but large errors appear in different positions around the nozzle, which could attribute to the abrasive flow dynamic condition changes with polishing time. This indicates that the variation of speed and pressure of abrasive flow should be considered as a polishing time function. The variation of the Preston model constant k_p during polishing should be investigated further for the understanding the CAJP performance.
5. It can be concluded that the material removal in CAJP is mainly conducted by the shearing and scratching actions. The tangentially aligned nozzle shroud in a constrained abrasive jet polishing process will improve material removal and surface roughness of workpiece.

Acknowledgements This work was supported by the National Natural Science Foundation of China (Grant No. 51305399, 51775509) and China Scholarship Council 201908330489.

Funding National Natural Science Foundation of China, 51305399, Qiaoling Yuan, 51775509, Qiaoling Yuan, China Scholarship Council, 201908330489, Qiaoling Yuan

Availability of data and material Relevant data have been given in the paper.

Declarations

Ethics approval The paper submission is in compliance with Ethical Standards.

Disclamer The authors have no financial or proprietary interests in any material discussed in this article.

Conflicts of interest There is no conflicts of interests.

References

1. Harvey JE, Lewotsky KL, Kotha A (1995) Effects of surface scatter on the optical performance of x-ray synchrotron beam-line mirrors. Appl Opt 34(16):3024
2. Zhao Q, Liang Y, Stephenson D, Corbett J (2007) Surface and subsurface integrity in diamond grinding of optical glasses on Tetraform 'C.' Int J Mach Tools Manuf 47(14):2091–2097
3. Zhao Q, Guo B (2015) Ultra-precision grinding of optical glasses using mono-layer nickel electroplated coarse-grained diamond wheels. Part 1: ELID assisted precision conditioning of grinding wheels. Precis Eng 39:56–66
4. Peng YF, Shen BY, Wang ZZ, Yang P, Yang W, Bi G (2021) Review on polishing technology of small-scale aspheric optics. The International Journal of Advanced Manufacturing Technology 115:965–987
5. Kordonski WI, Golini D (1999) Fundamentals of Magnetorheological Fluid Utilization in High Precision Finishing. J Intell Mater Syst Struct 10(9):683–689
6. Bingham RG, Walker DD, Kim DH, Brooks D, Freeman R, Riley D (2000) Novel automated process for aspheric surfaces. Proc. SPIE 4093, Current Developments in Lens Design and Optical Systems Engineering, International Symposium on Optical Science and Technology, 2000, San Diego, CA, United States. https://doi.org/10.1117/12.405237
7. Kordonski W, Golini D (2002) Multiple application of magnetorheological effect in high precision finishing. J Intell Mater Syst Struct 13(7–8):401–404

8. Bombard AJF, de Vicente J (2012) Thin-film rheology and tribology of magnetorheological fluids in isoviscous-ehl contacts. Tribol Lett 47(1):149–162
9. Ghosh G, Sidpara A, Bandyopadhyay PP (2021) Experimental and theoretical investigation into surface roughness and residual stress in magnetorheological finishing of OFHC copper. J Mater Process Technol 288:116899
10. Kumar JS, Paul PS, Raghunathan G, Alex DG (2019) A review of challenges and solutions in the preparation and use of magnetorheological fluids. International journal of mechanical and materials engineering 14(13):1–18. https://doi.org/10.1186/s40712-019-0109-2
11. Childs THC, Mahmood S, Yoon HJ (1994) The Material Removal Mechanism in Magnetic Fluid Grinding of Ceramic Ball Bearings. Proceedings of the Institution of Mechanical Engineers, Part B: Journal of Engineering Manufacture 208(1):47–59
12. Hashish M, Bothell D (1992) Polishing of CVD diamond films with abrasive liquid jets: an exploratory investigation. Proceedings SPIE Volume 1759, Diamond Optics V. https://doi.org/10.1117/12.130780
13. Fähnle OW, Brug H, Frankena HJ (1998) Fluid jet polishing of optical surfaces. Appl Opt 37(28):6771
14. Fähnle OW, van Brug HH (1999) Fluid jet polishing: removal process analysis, Proceedings in SPIE 3739, Optical Fabrication and Testing, Berlin, Germany, pp. 68–77. https://doi.org/10.1117/12.360189
15. Kordonski W, Shorey A (2007) Magnetorheological (MR) Jet Finishing Technology. J Intell Mater Syst Struct 18:1127–1130. https://doi.org/10.1177/1045389X07083139
16. Booij SM, van Brug H, Braat JJM, Fa¨hnle O.W. (2002) Nanometer deep shaping with fluid jet polishing. Opt Eng 41(8):1926–1931
17. Booij SM, Fähnle OW, Braat JJM (2004) Shaping with fluid jet polishing by footprint optimization. Appl Opt 43(1):67
18. Messelink WACM, Waeger R, Wons T, Meeder M, Heiniger KC, Faehnle OW (2005) Prepolishing and finishing of optical surfaces using fluid jet polishing. SPIE 2005:586908–586906
19. Matsumura T, Muramatsu T, Fueki S (2011) Abrasive water jet machining of glass with stagnation effect. CIRP Ann 60(1):355–358
20. Kalirasu S, Rajini N, Rajesh S, Jappes JTW, Karuppasamy K (2017) AWJM Performance of jute/polyester composite using MOORA and analytical models. Mater Manuf Processes 32(15):1730–1739
21. Wang Z, Li HN, Yu TB, Chen H, Zhao J (2019) On the predictive modelling of machined surface topography in abrasive air jet polishing of quartz glass. Int J Mech Sci 152:1–18
22. Dai Y (2009) Deterministic Magnetorheological Jet Polishing Technology. Ji xie gong cheng xue bao 45(5):171
23. Korobko EV, Mokeev AA, Kryt AV, Dragašius E, Mokeev AA (2018) Specific features of non-Newtonian magnetorheological fluid flow in the workpiece–instrument gap of a polishing facility. J Intell Mater Syst Struct 29(1):116–124
24. Wang T, Cheng H, Yang H, Wu W, Tam H (2015) Controlling mid-spatial frequency errors in magnetorheological jet polishing with a simple vertical model. Appl Opt 54(21):6433
25. Yang H, Cheng H, Feng Y, Jing X (2018) Removal of millimeter-scale rolled edges using bevel-cut-like tool influence function in magnetorheological jet polishing. Appl Opt 57(13):3377
26. US Deptartment of Energy (2016) DOE Fundamentals Handbook - Thermodynamics, Heat Transfer, and Fluid Flow (Volume 1 of 3), Lulu.com. ISBN: 1365110222, 9781365110221
27. Menter FR (1994) Two-equation eddy-viscosity turbulence models for engineering applications. AIAA J 32(8):1598–1605
28. Menter FR, Kuntz M, Langtry R (2003) Ten years of experience with the SST turbulence model. Turbulence, Heat and Mass Transfer 4, Hanjalic K., Nagano Y., and Tummers M., eds., Proceedings of the 4th International Symposium on Turbulence, Heat and Mass Transfer, Begell House Inc., Redding, CT, pp. 625–632
29. Ansari M, Nobari MRH, Amani E (2019) Determination of pitch angles and wind speeds ranges to improve wind turbine performance when using blade tip plates. Renewable Energy 140:957–969
30. Matthes N (2019) An algebraic characterization of the Kronecker function. Research in the Mathematical Sciences 6(3):1–13
31. Matyushenko AA, Garbaruk AV (2016) Adjustment of the k-ω SST turbulence model for prediction of airfoil characteristics near stall. J Phys 769:012082
32. Ji S (2011) Study on machinability of softness abrasive flow based on preston equation. Ji xie gong cheng xue bao 47(17):156
33. Makiuchi Y, Hashimoto F, Beaucamp A (2019) Model of material removal in vibratory finishing, based on Preston's law and discrete element method. CIRP Ann 68(1):365–368
34. Guo XG, Shi YT, Luo XC, Kang RK, Jin ZJ, Ding F, Li ZP (2019) Mechanism of crack propagation for K9 glass. Int J Precis Eng Manuf 20:815–825